# Tidal energy conversion in a global hot spot: On the 3-D dynamics of baroclinic tides at the Celtic Sea shelf break

Vlasenko, V

### RESEARCH ARTICLE

**Key Points:**
- Evidence of the largest internal waves ever recorded in the Celtic Sea
- Numerical replication of the three-dimensional fine structure of baroclinic tide
- Quasi-plane and spiral-type internal waves at the shelf edge of the Celtic Sea

# Tidal energy conversion in a global hot spot: On the 3-D dynamics of baroclinic tides at the Celtic Sea shelf break

**Vasiliy Vlasenko[1], Nataliya Stashchuk[1], Mark E. Inall[2], and Joanne E. Hopkins[3]**

[1]School of Marine Science and Engineering, Plymouth University, Plymouth, UK, [2]Scottish Association for Marine Science, Scottish Marine Institute, Argyll, UK, [3]National Oceanography Centre, Marine Physics and Ocean Climate, Liverpool, UK

**Abstract** Globally, the Celtic Sea shelf break is ranked highest as an energetic "hot spot" of tidal energy conversion, therefore making it the most significant contributor to global internal tidal energy flux. In this paper, the three-dimensional dynamics of baroclinic tides in the shelf-slope area of the Celtic Sea was investigated numerically and using observational data collected on the 376th cruise of the RV "RRS Discovery" in June 2012. The time series recorded at a shelf break mooring showed that semidiurnal internal waves were accompanied by packets of internal solitary waves with maximum amplitudes up to 105 m, the largest internal waves ever recorded in the Celtic Sea, and ranking among the largest observed in the global ocean. The observed baroclinic wavefields were replicated numerically using the Massachusetts Institute of Technology general circulation model. A fine-resolution grid with 115 m horizontal and 10 m vertical steps allowed the identification of two classes of short-scale internal waves. The first classification was generated over headlands and resembles spiral-type internal waves that are typical for isolated underwater banks. The second classification, generated within an area of several canyons, revealed properties of quasi-planar internal wave packets. The observed in situ intensification of tidal bottom currents at the shelf break mooring is explained in terms of a tidal beam that was formed over supercritical bottom topography at the mooring location.

## 1. Introduction

In situ data on internal tides reported in this paper were collected on the 376th cruise of the RV *RRS Discovery* (hereafter D376) in June 2012, in the slope-shelf area of the Celtic Sea (CS) (Figure 1, rectangle). The field campaign was conducted to study the processes controlling the cross-shelf transport on the NE Atlantic Ocean margin. The Celtic Sea continental slope is quite steep (typically 0.05 or steeper over the top 2000 m isobath), and contains a number of canyons and headlands [*Huthnance et al.*, 2001]. Tidal currents with typical mean velocities of 0.2 m s$^{-1}$ make an important contribution to turbulent energy production in the area. They enhance mixing in the bottom boundary layer where the barotropic tide feels the effects of bed friction, and also in the pycnocline where tidally generated internal waves can develop and dissipate. Internal waves are normally generated by tides over the shelf break [*Pingree and Mardell*, 1981, 1985; *Holt and Thorpe*, 1997], where they can dissipate or propagate away from the generation area making a significant contribution to midwater column mixing.

A number of field experiments have previously been conducted in the area. *Pingree and Mardell* [1981] reported on data recorded at two moorings, 001 (48.185°N, 7.9°W, depth 188 m) and 002 (48.28°N, 7.78°W, depth 163 m), deployed 13.5 km apart along a line perpendicular to the general shelf edge direction in September 1973. Their data revealed a series of the thermocline depressions at the shallowest of the two moorings (001); 3.2 h later these depressions developed into packets of internal solitary waves recorded at mooring 002. It was concluded that these internal waves did not propagate along the line connecting the two moorings, but within a sector between 20° and 40° to this line. In their successive work, *Pingree and Mardell* [1985] presented some further estimations of the characteristics of high-frequency internal waves propagating from the shelf break of the Celtic Sea in July 1983. The waves of depression were observed and classified as "parallel white walls" of water with amplitudes of more than 50 m.

*Holt and Thorpe* [1997] analyzed moorings deployed near La Chapelle Bank (47.5–47.6°N, 6.7–6.4°W), and also just inside our present study area (see Figure 1a). Based on this data set, the directions of
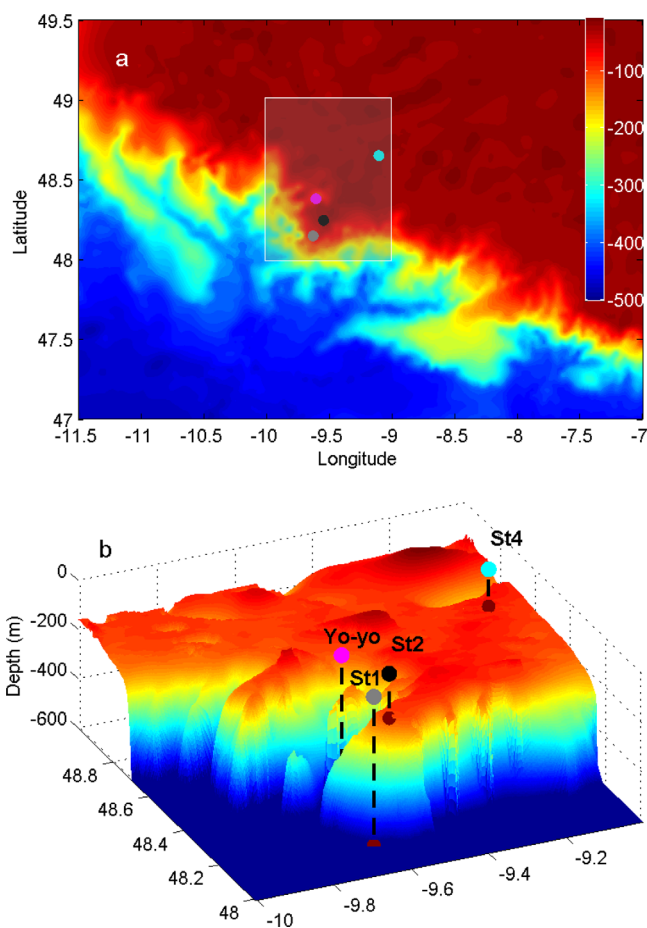
**Figure 1.** (a) Bathymetry of the Celtic Sea with positions of the yo-yo CTD station and three moorings St1, St2, and St4 deployed in the cruise. (b) Three-dimensional projection of the model domain shown in Figure 1a and used in modeling.

internal wave packet propagation were accurately quantified. They found that only a small number of the observed internal wave packets (from 20% to 30%) propagated in accordance with the generally accepted theoretical concept of their tidal nature, i.e., across the shelf-slope. All other packets were oriented quite randomly in space.

Summarizing the available historical data, one can conclude that the internal wavefield along the shelf edge area of the Celtic Sea is substantially three-dimensional. In our attempt to interpret the observational data collected on cruise D376, three-dimensional tidal modeling was used to replicate the characteristics of the internal waves. The paper is organized as follows: section 2 reports the data collected on D376, section 3 describes the model approach, and all basic model results are discussed in section 4. Lastly, section 5 provides a discussion and draws our conclusions.

## 2. Field Experiment

### 2.1. Instruments

The observational campaign of cruise D376 to the Celtic Sea in June 2012 included CTD surveys (not discussed here) and the deployment of three moorings: St1, St2, and St4 (shown in Figure 1b). Moorings St1 (48°08.812′N; 09°37.798′W; depth 680 m, 12–28 June 2012) and St2 (48°14.660′N; 09°32.780′W; depth 184 m, 13–28 June 2012) were deployed on the steep slope and shelf break, respectively, with the aim of quantifying the characteristics of baroclinic tides close to the site of their generation. Data from Mooring St4 (48°38.098′N; 09°06.363′W; depth 156 m, 16–28 June 2012) deployed further onto the shelf in shallower water, approximately 30 km from the shelf-slope generation area, were used for setting the tidal forcing in the MITgcm.

Each mooring was equipped with a string of top to bottom thermistors sampling at 1 min intervals. Instruments were spaced between 1 and 2.5 m within the thermocline. In the bottom mixed layer, the spacing was increased to 10–20 m at St2 and St4, and up to 50 m at St1. All temperature loggers were cross-calibrated before and after deployment to correct for any drifts and offsets. Additionally, all the mini-temperature loggers were calibrated against the ships CTD. Either bottom mounted or in-line ADCPs recorded 1 min ensemble currents at each site, within 2 m bins at St2 and St4, and 8 m bins at St1. Current direction at each mooring was corrected for magnetic variation and any measurements owing to contamination by strong sea-surface echos removed.

### 2.2. Data

The bottom topography in the observational domain is rather complicated. A number of canyons and headlands makes it highly corrugated (see Figure 1) suggesting a substantially three-dimensional structure of
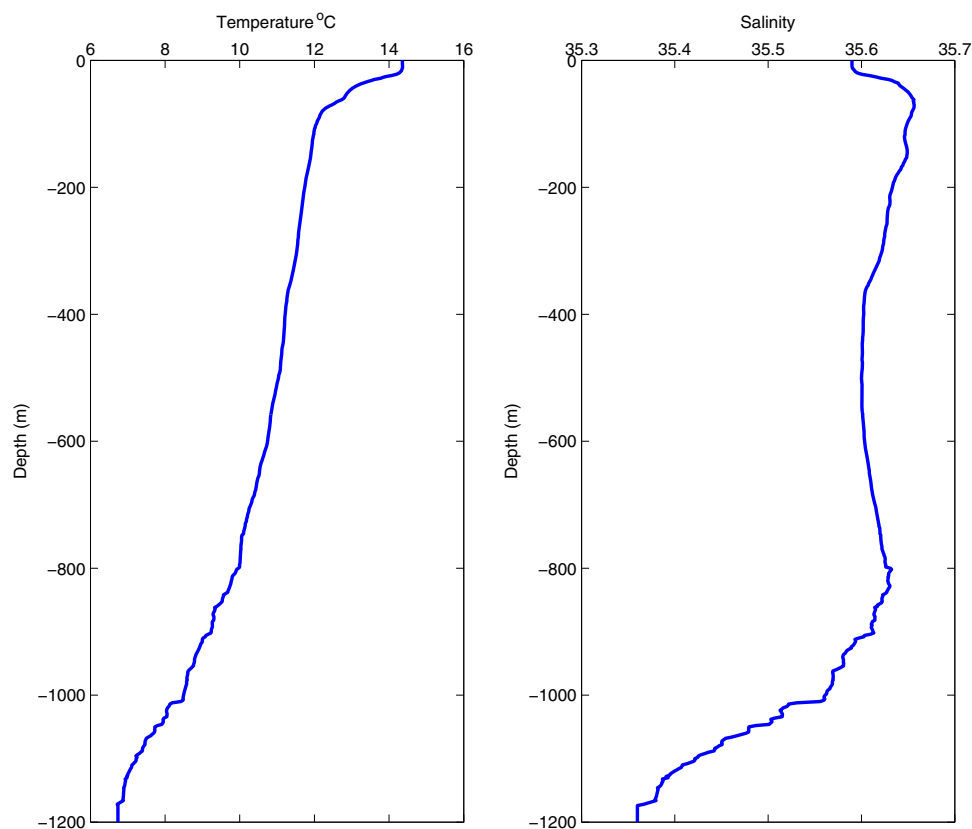
**Figure 2.** Averaged profiles of (a) temperature and (b) salinity recorded at the yo-yo CTD station.

the baroclinic wavefields in the area. In terms of tidal energy conversion, apart from the bottom topography, two other parameters control the intensity of the generated baroclinic tides; the barotropic tidal forcing and vertical fluid stratification. The latter, in fact, is highly sensitive to the dynamical processes developing in the area that can deviate isopycnals, specifically large-amplitude internal waves. To minimize the influence of high-frequency noise and to get statistically justified undisturbed vertical profiles of salinity and temperature, the data from 12 yo-yo CTD stations (29 June 2012 13:01–30 June 2012 03:40) around the point (48°22.5′N; 09°37.5′W; depth 1200 m, Figure 1) were averaged (see Figure 2). The stratification is mostly controlled by the temperature that decreases from 14.5°C at the free surface to 6.5°C at a depth of 1200 m. The profiles of Figure 2 show that the seasonal pycnocline was located in a 50 m thick subsurface layer (between 20 and 70 m), which is quite shallow and thus a weak baroclinic response to the tidal forcing might be assumed [*Vlasenko et al.*, 2005].

The moorings were deployed during the last 2 weeks of June 2012, for between 11.9 and 15.3 days. It is clear from the vertically averaged ADCP time series recorded at moorings St1 (depth 680 m) and St4 (depth 180 m) and presented in Figure 3 that tidal velocities were in the range $\pm 0.1$ m s$^{-1}$ for the deep water mooring and $\pm 0.4$ m s$^{-1}$ for the shallow mooring. For the analysis and model comparison, we choose the best recorded and most representative (in terms of the baroclinic tidal signal) 2 day period (days 177.2–179.2 of year 2012, or 25–27 June 2012).

The thermistor chain record at St1 (see Figure 4a) contains a superposition of a long-term semidiurnal tidal wave with a number of short-period internal solitary waves. The latter were recorded as a series of internal wave packets riding a long-term periodic tidal wave shown in Figure 4a by a dashed line. The amplitude of the semidiurnal vertical pycnocline displacements reached 10 m (with a total trough-to-crest range of 20 m), which may be considered a reasonably strong internal tidal response. A number of spikes shown in Figure 4a, associated with short-period internal solitary waves, had even larger amplitudes. For instance, the
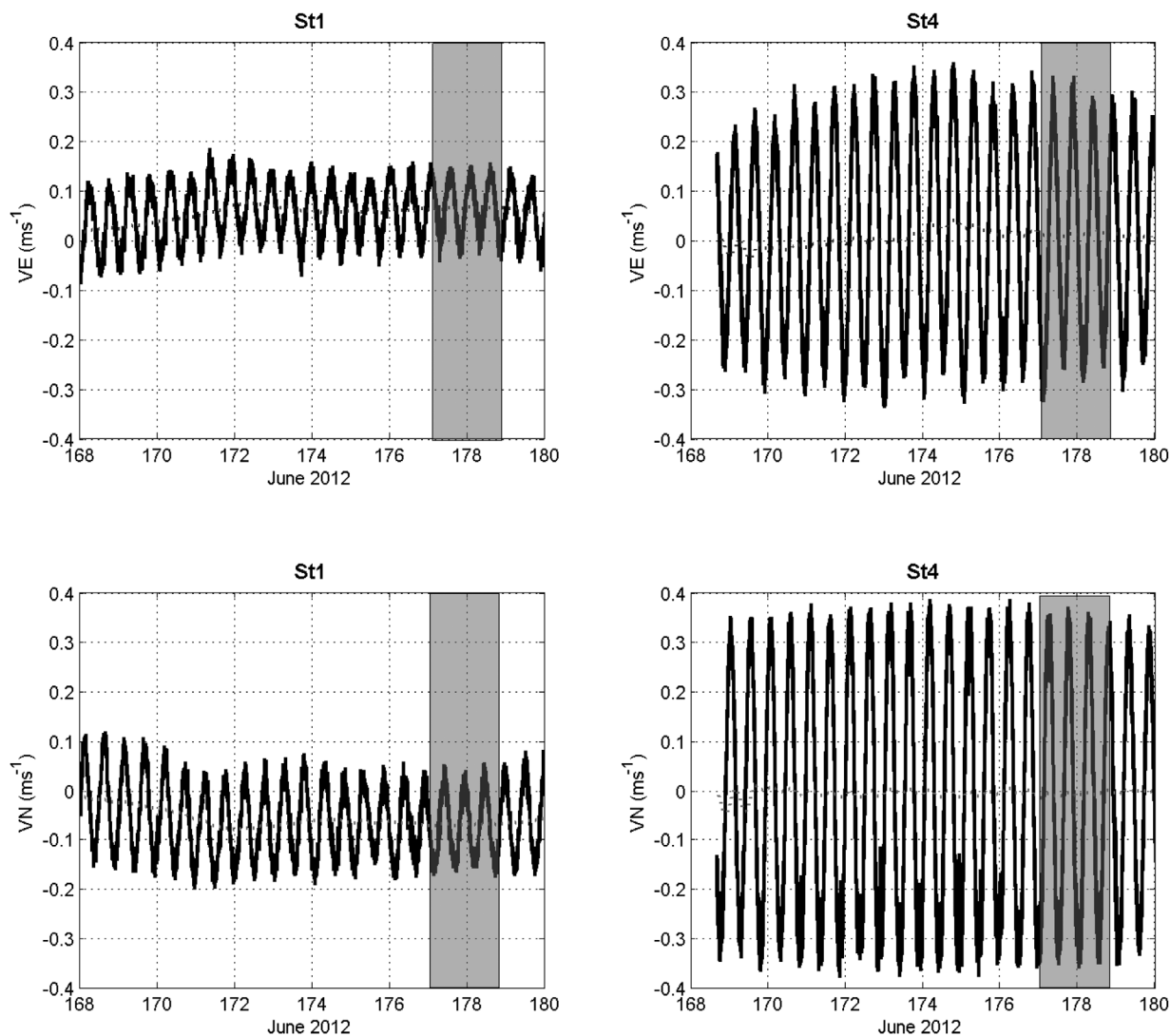
**Figure 3.** (top) Zonal and (bottom) meridional vertical averaged tidal velocities from ADCP at the positions of moorings St1 (left column) and St4 (right column). The shaded rectangles depict the time interval analyzed in this paper.

amplitude of the leading wave in the packet recorded on days 177.25–177.60 of year 2012 was estimated to be 105 m, which can be considered as the largest internal wave ever observed in the Celtic Sea. This wave packet is shown more closely in Figure 5.

Figures 4b and 4c show the eastward and northward ADCP velocities, respectively. Both horizontal velocities reveal quite strong semidiurnal periodicity. Obviously, these time series contain both barotropic and baroclinic tidal signals. The most intriguing feature of the recorded data at this location is the intensification of the tidal currents near the bottom.

Figure 6 still provides some evidence of a long-term semidiurnal periodicity with vertical oscillations of the isotherms up to 70 m (see Figure 6a, time span 178.5–179.2 day of year 2012), however, the short-term oscillations here are not as regular as those at St1. They are mostly randomly distributed along the whole time series.

It is clear that the origin of the internal waves recorded at moorings St1 and St2 cannot be reliably inferred from just two mooring records alone. This can, however, be achieved through accurate 3-D modeling of the baroclinic tides using the available data set to guide the correct choice of model parameters and as a bench mark for model validation.
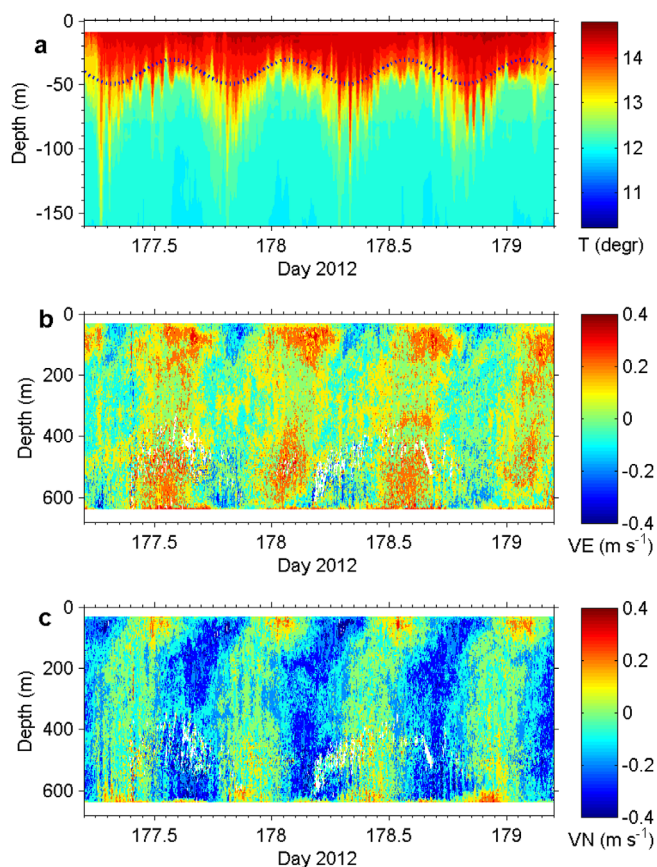
**Figure 4.** (a) Temperature, (b) zonal, and (c) meridional velocities recorded at the mooring St1. Dotted blue line in the top plot depicts semidiurnal oscillation of the thermocline.

## 3. Numerical Model

The numerical modeling of baroclinic tides was conducted using the Massachusetts Institute of Technology general circulation model (MITgcm) [*Marshall et al.*, 1997]. A fine-resolution grid with a horizontal step of 115 m in both the meridional and zonal directions was used to cover the calculational domain shown by the rectangle in Figure 1a. Some extra-grid points with a two-step telescopic increase of the horizontal resolution from 115 m to 100 km at the periphery were added to the lateral boundaries. The first, starting at the liquid boundaries (the rectangle in Figure 1a) had quite a gentle telescopic grid stretching that allowed for propagation of all internal waves through the liquid boundaries without reflection. In the outer area, a sharper increase of the grid resolution allowed surface waves to propagate quite a long distance from the central domain without any backward reflection. Thus, the combination of the two telescopes, one for internal and another for surface

waves, guaranteed an accurate numerical solution within the internal model domain without any signals reflected from the boundaries during at least 10 tidal cycles. In the vertical direction, the grid size was also variable, viz. 10 m in the upper 200 m surface layer below which it was increased to 25 m.

Tidal forcing was initialized in the model by setting some extra periodical terms in the right hand side (RHS) of the momentum balance equations. The target was to reproduce the barotropic tides predicted by any other tidal model. The parameters of the external forcing (semidiurnal tidal potential in the RHS of momentum balance equations) were set in such a way so as to get the best fit of the MITgcm barotropic output (calculated for a homogeneous fluid) to the vertically averaged tidal velocities for the period 25–27 June 2012 (rectangle in Figure 3). The tidal ellipses from MITgcm shown in Figure 7 were consistent with the TPXO7.1 output [*Egbert and Erofeeva*, 2002] (the TPXO data are freely available from http://volkov.oce.orst.edu/tides/). A vertical stratification was introduced into the model after setting the tidal forcing for a homogeneous fluid. The temperature and salinity profiles were taken from the direct CTD measurements at the yo-yo stations conducted in the area of the shelf break (Figure 2).

As mentioned above, large-amplitude internal solitary waves are generated in the area on a regular basis. They normally produce strong shear and mixing. A standard procedure to cope with the numerical instability in this case and to provide the necessary level of mixing is to use the Richardson number-dependent parameterization for vertical viscosity $\nu$ and diffusivity $\kappa$ introduced in *Pacanowski and Philander* [1981]:

$$\nu = \frac{\nu_0}{(1+\alpha\mathrm{Ri})^n} + \nu_b, \quad \kappa = \frac{\nu}{(1+\alpha\mathrm{Ri})} + \kappa_b.$$

Here $\mathrm{Ri} = N^2(z)/(u_z^2 + v_z^2)$ is the Richardson number, $u$ and $v$ are the components of horizontal velocity; $N(z) = \sqrt{-g/\rho(\partial\rho/\partial z)}$ is the buoyancy frequency, where $g$ is the acceleration due to gravity and $\rho$ is the water
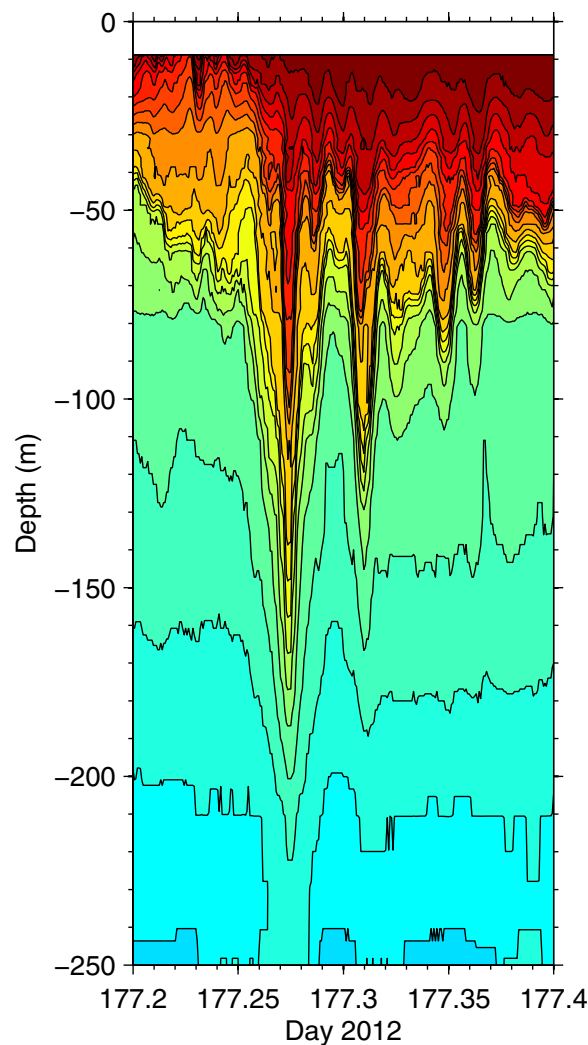
density; $v_b = 10^{-5}$ m$^2$ s$^{-1}$ and $\kappa_b = 10^{-5}$ m$^2$ s$^{-1}$ are the background viscosity and diffusivity, respectively; $v_0 = 1.5 \times 10^{-2}$ m$^2$ s$^{-1}$, $\alpha = 5$, and $n = 1$ are the adjustable parameters. Such a parameterization increases $v$ and $\kappa$ in areas where the Richardson number is small. The horizontal viscosity and diffusivity were set to a constant value of 0.5 m$^2$ s$^{-1}$.

## 4. Model Results

### 4.1. Comparison With Observations

To perform a comparative analysis of the model output with the observational data, two virtual "numerical moorings" with positions similar to St1 and St2 were activated in the code to provide the temperature and salinity time series with a 1 min sampling interval, similar to that recorded at moorings St1 and St2. Figures 8 and 9 show the temperature (a), and the eastward and northward velocities (b and c, respectively) obtained numerically for the positions of the moorings St1 and St2. The model predicted temperature oscillations at St1 (Figure 8a) reveals quite a good qualitative and quantitative consistency with the in situ time series (Figure 4a). Indeed, a very strong long-period semidiurnal signal with 20 m vertical thermocline displacements recorded at St1 was accurately reproduced by the model. Moreover, similar to the in situ data, the model predicts a series of higher frequency vertical displacements, presumably produced by packets of internal solitary waves, in the trough of the internal tidal wave. The arrival time of these internal wave packets at the mooring St1 coincide with their observational counterparts, testifying the ability of the model to capture all basic characteristics of the waves observed at mooring St1. The numerical soliton amplitudes were slightly smaller than their experimental counterparts partly because of the numerical viscosity that affects mostly the short-scale waves.



**Figure 5.** Fragment of the temperature time series recorded at St1 showing the maximum internal solitary waves passing the mooring.

To make the comparative analysis more quantitative, the correlation coefficient ($r$) between modeled and observed vertical isotherm displacements was calculated according to the formula:

$$ r = \frac{\sum_{i=1}^{n}(P_i - \bar{P}) \sum_{1}^{n}(O_i - \bar{O})}{\sqrt{\sum_{i=1}^{n}(P_i - \bar{P})^2 \sum_{i=1}^{n}(O_i - \bar{O})^2}}. $$

Here $P$ is the model predicted displacement of the isotherm from its equilibrium depth, $O$ is the observed displacement recorded at mooring St1, and overbar denotes averaging over $n$ readings. Two-day time intervals shown in Figures 4a and 8a were taken for the comparison. The correlation coefficient $r$ between model predictions and observed time series recorded on days 178 and 179 of year 2012 are shown in the left part
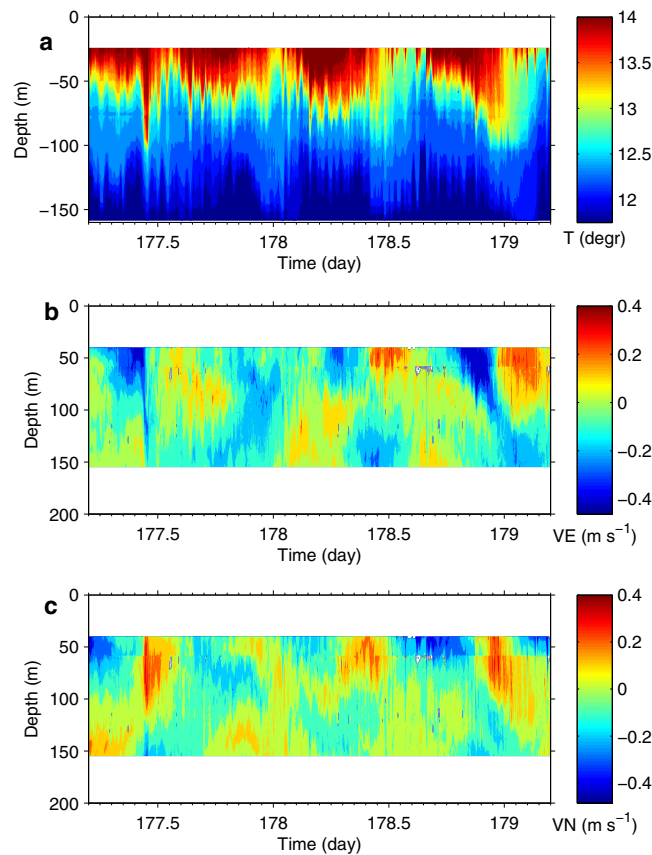
**Figure 6.** The same as Figure 4, but for the mooring St2.

of the Table 1. In order to give some reference value of $r$, the correlation coefficient between days 176–177 and days 178–179 from the observational data was also calculated.

It is clear from Table 1 that the consistency between the model output and observational data is fairly good, especially in the thermocline layer where the baroclinic tidal signal was strong. The correlation coefficient here between model and observations is even higher than between two different observational periods. The correlation decreases downward due to a weaker stratification in the bottom layers where the specific contribution of the noise to the total baroclinic signal is higher.

Another quantitative measure of the model performance is the index of agreement introduced by *Willmott* [1981, 1982]:

$$d = 1 - \frac{\sum_{i=1}^{n}(P_i - O_i)^2}{\sum_{i=1}^{n}(|P_i - \bar{P}| + |O_i - \bar{O}|)^2},$$

a measure of the extent to which the model output is error free. The coefficient $d$ can vary from 0 (complete disagreement between predicted and observed values) to 1 (perfect coincidence). It is presented in the right part of Table 1. Similar to the correlation coefficient, the observed time series recorded on days 178 and 179 are compared against the model output, as well as against the observational time series recorded 2 days earlier, i.e., on days 176–177 of year 2012. A good consistency with observations is demonstrated by the model in the thermocline layer that reduces to a half in the weakly stratified layer.

Comparison of the model velocity time series (Figures 8b and 8c), with the observational current record at St1 (Figures 4b and 4c) reveals good agreement in speed, magnitude, and structure. It is interesting that both time series (theoretical and recorded in situ) reveal similar intensification of the tidal currents near the bottom (below 600 m).

The model output for mooring St2 is shown in Figure 9. Similar to the observed temperature field (Figure 6a), the predicted temperature time series at St2 (Figure 9a) is less regular than that at St1 (see Figure 8a). Unlike the situation at St1, it cannot be easily approximated by a single sine wave (see Figures 4a and 8a), although the tidal periodicity is still clearly visible (Figure 9a). Note also that as in the field experiment (Figure 6a) the modeled time series reveal weaker high-frequency internal wave activity (Figure 9a) than was observed. Comparison of the predicted velocity time series (Figures 9b and 9c) with the available in situ observations at St2 (Figures 6b and 6c) qualitatively demonstrate their consistency, both in the velocity range, and in the absence of the intensification of the tidal currents in the bottom layer.

Thus, the model validation shows that all basic wave characteristics recorded in situ at moorings St1 and St2 were replicated by the model quite successfully, both for low-frequency tidal oscillations, and for high-frequency internal waves. Consistency of the model output with the observational data at the
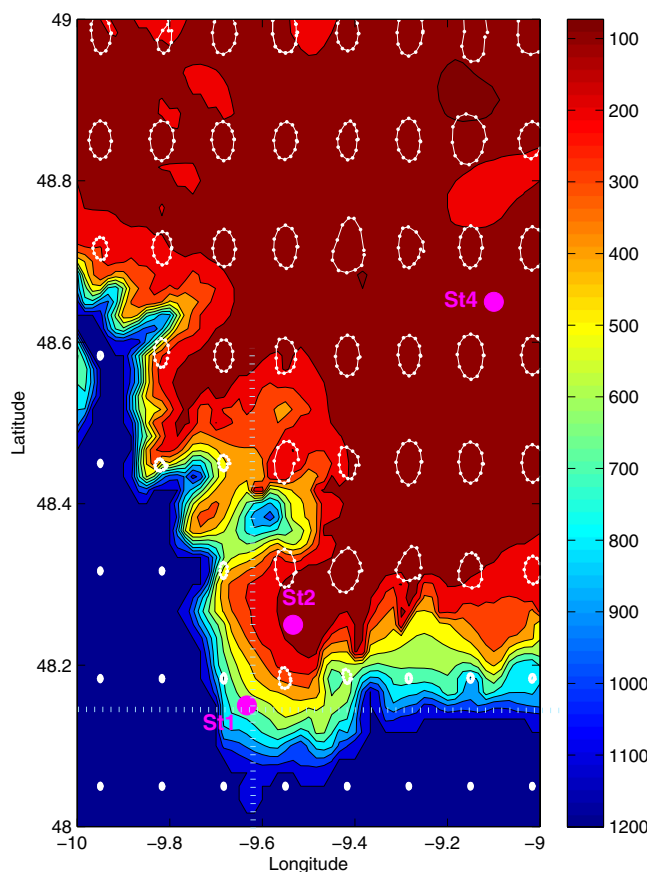
**Figure 7.** MITgcm predicted barotropic tidal ellipses for 25–27 July 2012.

moorings allows one to use it for further analysis of the three-dimensional structure of the baroclinic tidal field across the whole domain.

### 4.2. 3-D Generation

Model predictions of the surface elevations and depressions produced by internal solitary waves (i.e., the surface signature of internal waves) were used for three-dimensional spatial tracking of the wavefronts. A strong internal wave of depression with an amplitude of several tens of meters produces a free surface elevation of a few centimeters located immediately above the wave trough; waves of elevation generate a depression at the free surface. An example of such a free surface wave signature presented in Figure 10 shows that the structure of the wave pattern is quite complicated, and indeed is reminiscent of satellite Synthetic Aperture Radar (SAR) images of the area [*Jackson and Apel*, 2002]. It resembles a superposition of a series of packets of short-scale internal waves (circular and quasi-planar) radiating from different fragments of the shelf break.

Figure 10 shows just one specific wave pattern. To reconstruct the whole picture of internal wave dynamics in the area, i.e., the evolution of the wave structure, a series of model outputs is analyzed. Figure 11 represents overlaid signatures of all the strongest wave systems during one and a half tidal cycles (only the leading waves in every packet are shown). One hour temporal steps between two successive frames were used to construct this picture. The number on every wavefront depicts the time in hours after the beginning of the numerical run. The waves that were apparent for less than 3 h were omitted from the analysis. In order to simplify the visual presentation of all the wave systems, they are shown in Figure 11 in two plots, and every system is represented by a unique color. Comparing the spatial structure of all waves, one can identify two classes of generated internal waves. Waves of the first class shown in black in Figure 11a reveal the properties of spiral-type internal waves similar to those observed in the area of Jones Bank [*Vlasenko et al.*, 2013] and generated over an isolated Gaussian-type underwater bank discussed in Appendix A. The position of their generation is identified as the top of the headland, coincident with the location of mooring St2 (compare the wavefronts at *t* = 28, 29, and 30 h). This wave structure rotates clockwise and in fact is a combination of several fragments that ultimately merge into a single wave system (black and red wavefronts in Figure 11a that existed separately prior to *t* = 38 h, but then merged and propagated together). A similar spiral wave system, shown in Figure 11b by the dark-brown contours, was detected near a steep, isolated, elongated, and seaward protruding spur, a topographic feature having the same effect as an isolated bank.

Waves falling into the second class are quite different in their spatial characteristics. The northernmost canyon shown in Figure 11 is a source of two systems of waves (blue color): the strongest one propagates shoreward (Figure 11b) as a superposition of two initially radially spreading packets that merge after *t* = 29 h and then move forward together as a single wavefront. Another wave system (Figure 11a) is generated at the southern
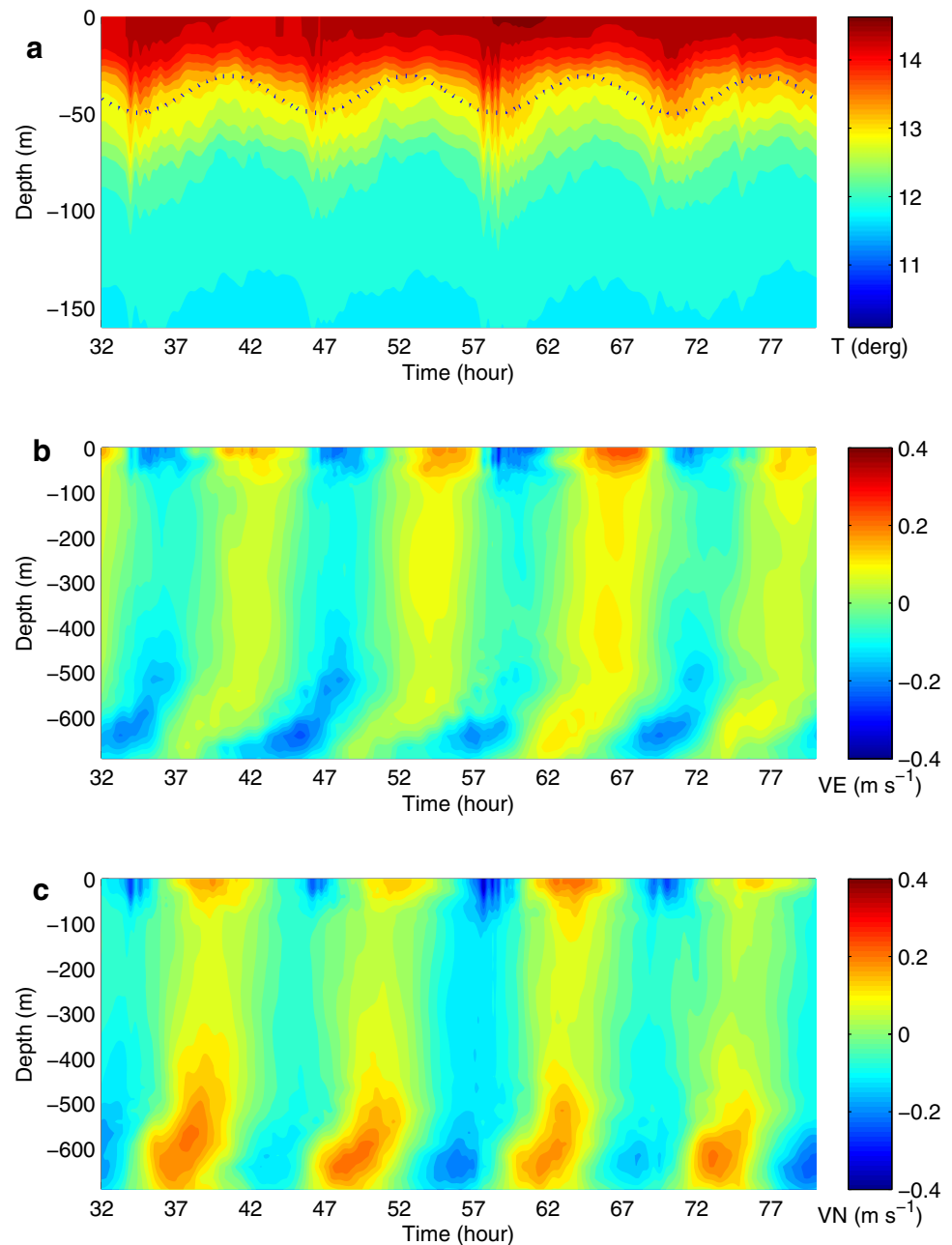
**Figure 8.** Model predicted (a) temperature, (b) eastward, and (c) northward velocity components for the moorings St1.

flank of the canyon and propagates to the west. The tides around the system of canyons to the east of St2 generate waves that propagate in the north-east and eastern directions. They are shaded light brown in Figure 11.

The analysis of sea-surface signatures allows one to specify many details of the spatial evolution of short-scale internal waves. Note, however, that with this approach it is not always possible to detect all the sources of tidal energy conversion. This is because the short-scale internal waves presented in Figures 11 and 12 are not always visible near the source of their generation or they are not generated at all due to weak tidal forcing. As such an alternative means of detecting the sources of baroclinic tidal energy can be based on the concept of the linear internal body force (IBF) developed by *Baines* [1982]. The details of this methodology are described in Appendix B. Figure 12 shows the result of its application within the study area. The procedure for mapping
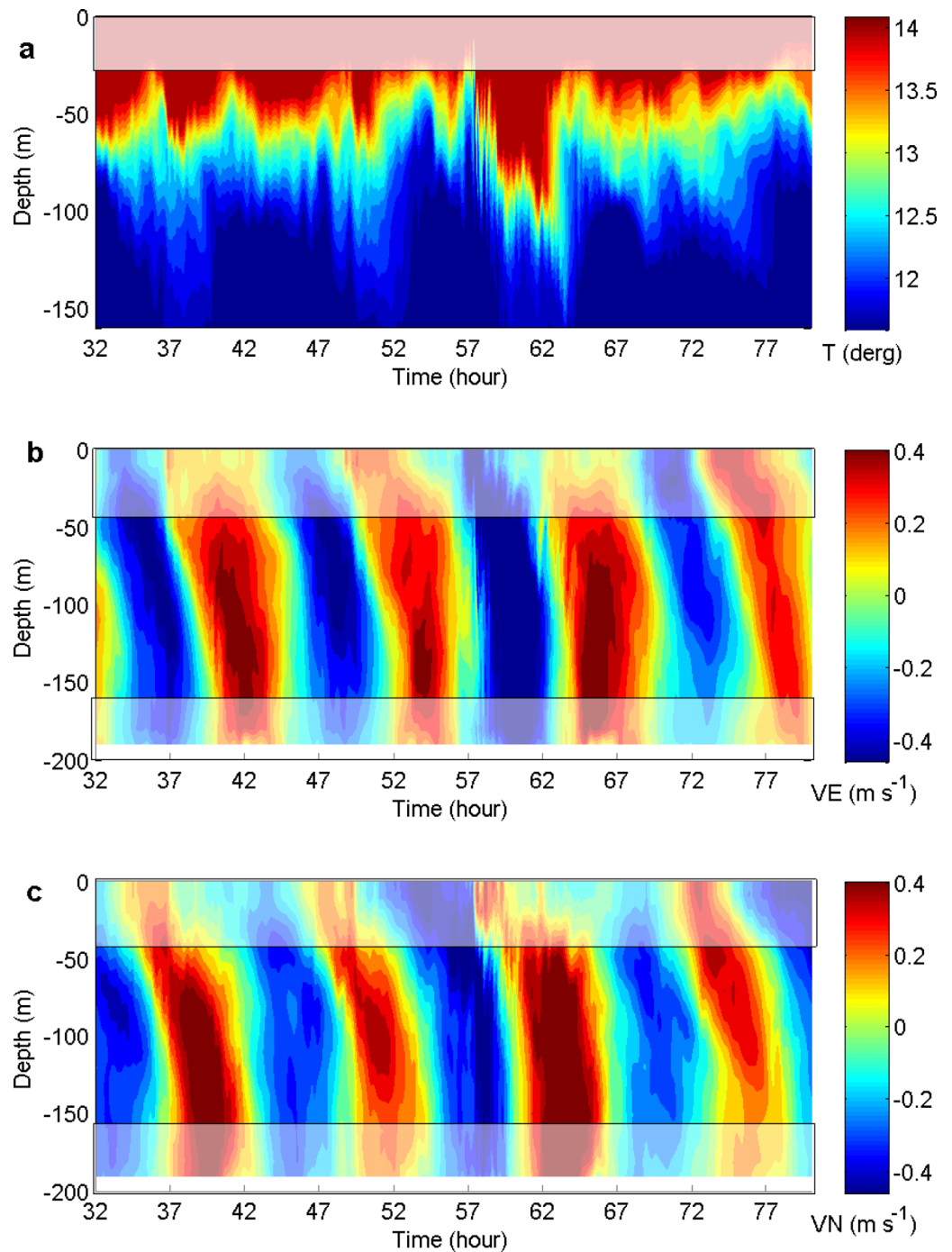
**Figure 9.** The same as in Figure 8, but for the mooring St2.

the IBF is as follows. The total value of the IBF function integrated over the whole model domain is taken as 100%. The green color shows the areas with maxima IBF within which 10% of the total spatially integrated IBF are located. The yellow color in Figure 12 shows the areas where 50% of the tidal energy conversion are located. As can be seen from the IBF distribution, the linear theory predicts that the barotropic tidal energy is converted into the baroclinic component in some restricted areas that are not necessary located over the shelf break.

Combined analysis of all basic wave systems predicted by the MITgcm (Figure 11), and the IBF distribution (Figure 12), allows a mapping of the areas of wave generation. The latter is shown in Figure 12 using the

**Table 1.** The Correlation Coefficient (*r*) and the Index of Agreement (*d*) Between Modeled and Observed Vertical Isotherm Displacements at St1 for Days 178–179 of Year 2012 (2nd and 4th Columns), and Observed Vertical Displacements on Days 176–177 and 178–179 (3rd and 5th Columns)[a]

| | Correlation Coefficient (*r*) | | Index of Agreement (*d*) | |
|---|---|---|---|---|
| Isotherm (Mean Depth) | Model Versus Observations 178–179 | Observations 176–177 Versus Observations 178–179 | Model Versus Observations 178–179 | Observations 176–177 Versus Observations 178–179 |
| 13.5°C (31 m) | 0.68 | 0.43 | 0.65 | 0.64 |
| 13.0°C (46 m) | 0.70 | 0.55 | 0.69 | 0.73 |
| 12.5°C (67 m) | 0.70 | 0.60 | 0.68 | 0.75 |
| 11.5°C (313 m) | 0.54 | 0.55 | 0.48 | 0.73 |
| 11.0°C (507 m) | 0.32 | 0.36 | 0.51 | 0.54 |

[a]The compared isotherms and their averaged depths are shown in the first column.

same colors as the wave signatures in Figure 11. Comparing the wave signatures predicted by the fully non-linear nohydrostatic MITgcm with the places of possible wave generation revealed by the linear IBF-methodology, one can conclude that there is good consistency even though the latter does not specify the details of the spatial evolution of the waves generated.

### 4.3. Bottom Intensification

The time series recorded in situ and predicted by the model at the mooring St1 revealed an intensification of the tidal currents in the bottom layer over the headland (Figures 4b, 4c and 8b, 8c). The intensification extended 100 m above the bottom and was quite persistent over the whole observational period. It is interesting that similar intensification was not predicted by the model at mooring St2 (Figures 9b and 9c), just 11 km away.

The reason for this local intensification can be explained in terms of the generation of tidal beams. Figure 13 depicts the maxima of the horizontal velocities over one tidal cycle in zonal (Figure 13a) and meridional (Figure 13b) cross sections through the mooring St1. A baroclinic tidal beam is clearly seen at the top of the local topography where the mooring St1 was deployed and extends to the abyss along the line

$$z = \sqrt{(\sigma^2 - f^2)/(N^2(z) - \sigma^2)}\,x + \text{const} ,$$

which is the line of propagation of the M2 tidal internal wave energy (here $\sigma$ is the semidiurnal
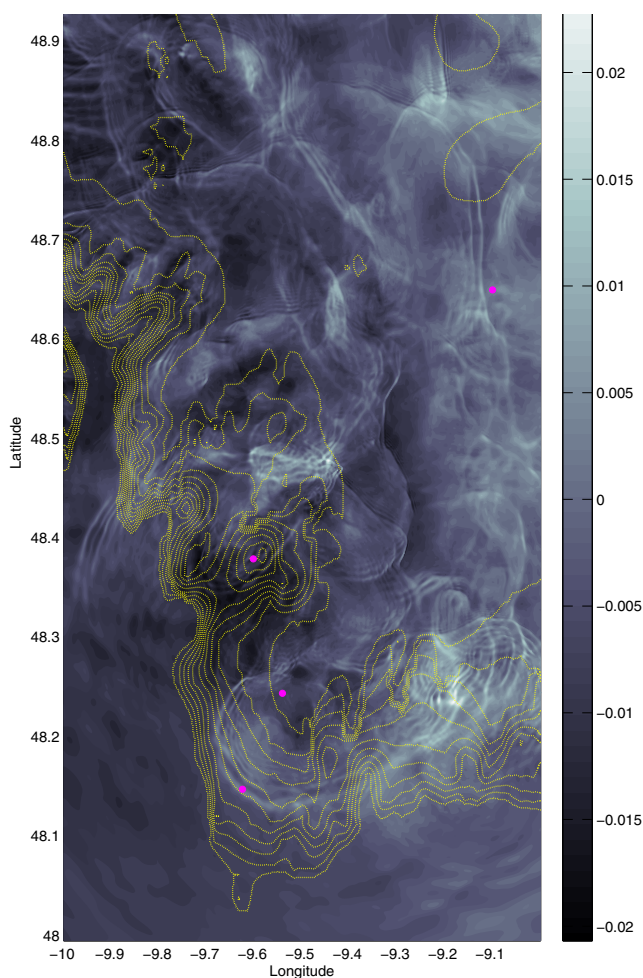


**Figure 10.** Model predicted see surface elevations (light color) generated by internal waves after 34 h of the model run. The colorbar shows values in m.
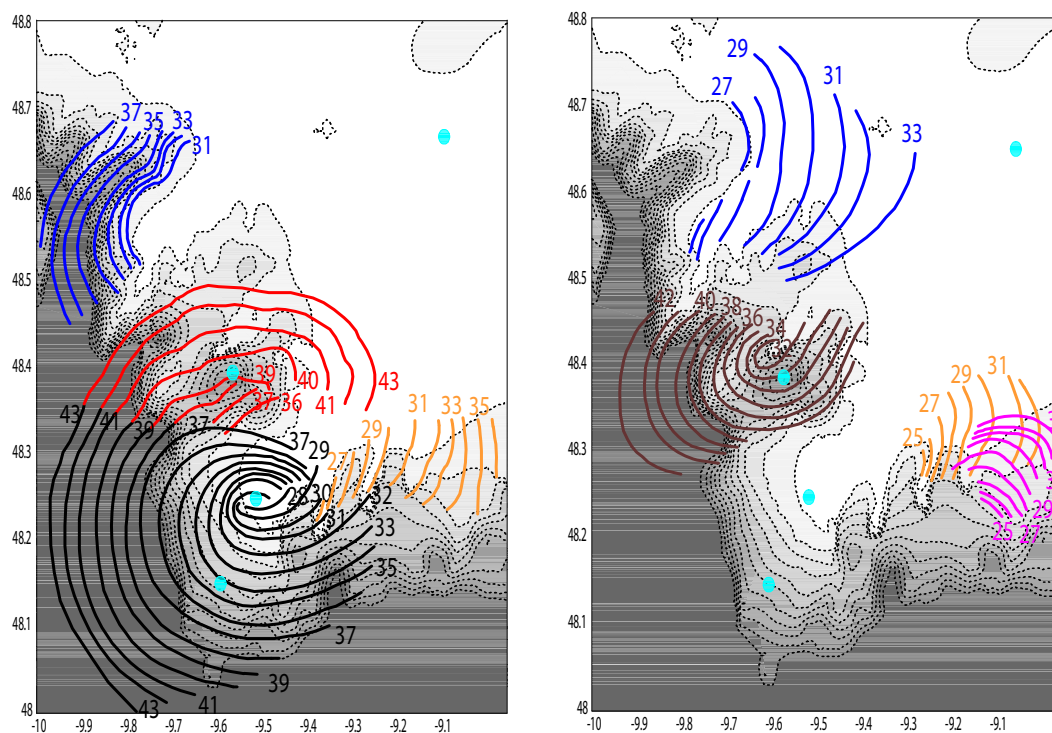
**Figure 11.** Evolution picture of the strongest wave systems generated in the area. The numbers on the wavefronts depict the time (in h) after the beginning of the experiment.

frequency, $f$ is the Coriolis parameter). In fact, this is the characteristic line of a two-dimensional hyperbolic wave equation which in the three-dimensional case takes the form of a conical surface. It is clear from Figure 13 that the local topography is steeper than the characteristic line, which creates favorable conditions for the generation of a baroclinic tidal beam. By chance, the mooring St1 was deployed just at the point of its formation, which made it possible to record the origin of the tidal beam directly.

## 5. Discussion and Conclusions

In summarizing the main findings of this study on the baroclinic tidal dynamics of the Celtic Sea, one should mention the role that this region plays in global tidal energy conversion. In his seminal work, *Baines* [1982] first classified the 12 most energetic areas of tidal energy conversion in the Global Ocean. In this classification, based on a two-dimensional linear hydrodynamic model, the Celtic Sea shelf break ranked highest as an energetic "hot spot" therefore making the most significant contribution to global internal tidal energy flux. Note, however, that since then observational effort has mostly been attracted to other sites of the World Ocean where gigantic internal solitary waves with amplitudes up to 100 m or more have been observed: most notably, the Andaman Sea [*Osborne and Burch*, 1980], South China Sea [*Farmer et al.*, 2009], and the Straits of Gibraltar [*Wesson and Gregg*, 1994; *Bruno et al.*, 2002; *Vlasenko et al.*, 2009]. In this respect, much less attention has been paid to the Celtic Sea, and only a few papers reporting observations of large-amplitude ISWs have been published [see, for instance, *Pingree and Mardell*, 1981, 1985; *Holt and Thorpe*, 1997]. Significant progress in greater recognition of the role of the Celtic Sea was achieved in June 2012 and is reported here. The amplitude of the strongest internal solitary waves (ISW) observed in this cruise exceeded 100 m. One of the examples is shown in Figure 5 where ISW with the amplitude of 105 m is presented. The amplitudes of many others short waves were well above 50 m, see Figure 4a.

A detailed analysis of the generation conditions of these waves, their spatial structure, and dynamics was conducted using the advanced nohydrostatic MITgcm. For these numerical experiments, the observational
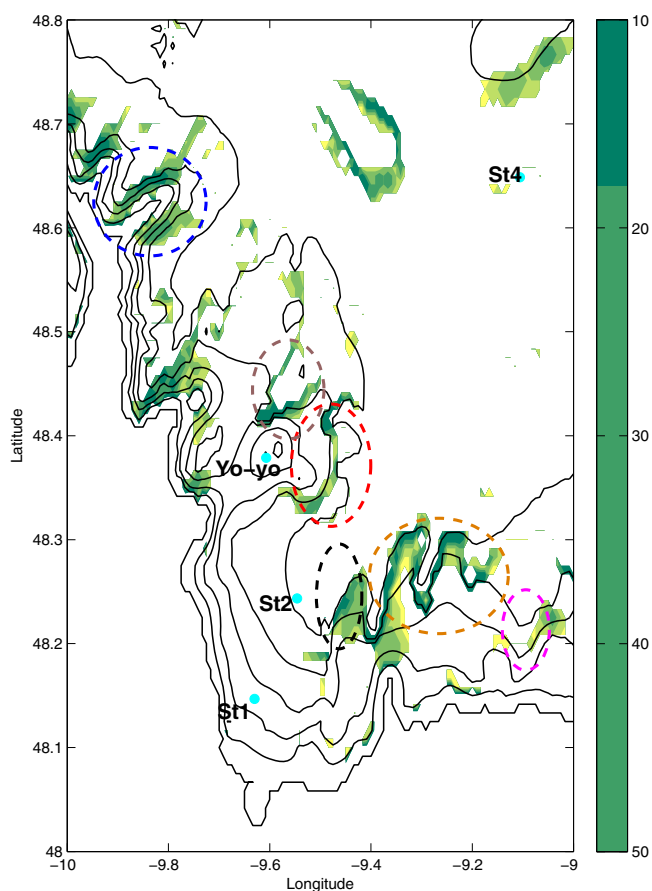
**Figure 12.** Distribution of the internal body force Φ in the slope-shelf area of the Celtic Sea. Ellipses mark the position where waves presented in Figure 11 were generated. The color of the ellipses corresponds to the wave color in Figure 11.

data collected during cruise D376 in June 2012 were used as a benchmark for the model validation. Based on the results of the numerical modeling, it was possible to localize all the main sources of tidal energy conversion. Surprisingly, the IBF methodology developed by *Baines* [1982] gives quite a serviceable result, i.e., most of the sources of the baroclinic tidal energy conversion detected using the fully nonlinear nohydrostatic MITgcm were also predicted by the linear methodology. As a result, the IBF method can be used for some future practical applications that are mostly concerned with mapping of the sources of tidal energy conversion, but not the detailed structure of the wavefield. With respect to the latter, the MITgcm allowed for the identification of two classes of tidally generated internal waves, viz. quasi-plane ones originating from the local canyons (Class 1), and spiral-type waves generated over headlands (Class 2).

In terms of the Froude number analysis, the generation mechanism of these waves in the shelf break area can be classified as subcritical. The phase speed of the first-mode short-scale internal waves in the area of the generation of spiral-type internal waves, i.e. at the position of the mooring St2 (depth 184 m), was in the range between 0.3 and 0.35 m s$^{-1}$ (calculated from a standard boundary value problem) which is more than 1.5 times larger than the amplitude of the tidal current estimated here as 0.2 m s$^{-1}$ (see Figure 6). As a result, generated over the shelf break and propagated from the sources of generation internal waves steepen and disintegrate into packets of short-scale large-amplitude internal solitary waves. Such a transformation over quite a short distance between two moorings (13.5 km) was reported previously by *Pingree and Mardell* [1981].

Overall, the spatial structure of generated internal waves was substantially three-dimensional. In contradiction to a commonly accepted concept that the cross-shelf flux of baroclinic tidal energy is controlled by a general direction of the shelf break [*Garrett and Kunze*, 2007], the waves generated in the Celtic Sea propagated in all directions, both perpendicular to the shelf break and along it. Some tens of kilometers shoreward of the shelf break, and away from the complexity of the generation region discussed in this article, however, there is observational evidence that the quasi-linear sinusoidal component of the internal tide does propagate shoreward as a coherent planar wave [*Inall et al.*, 2011; *Pingree and New*, 1995].

Such a chaotic propagation was reported before by *Pingree and Mardell* [1981] and *Holt and Thorpe* [1997]. From the modeling point of view, the basic reason for this is substantial three-dimensionality of the bottom topography which contains a number of canyons and headlands.

In terms of the mechanism of tidal energy conversion, the regime of wave generation in the Celtic Sea study area can be classified as supercritical, i.e., the bottom topography is steeper than trajectories of propagating internal waves. As a result, the generation of a tidal beam is expected. This is confirmed by
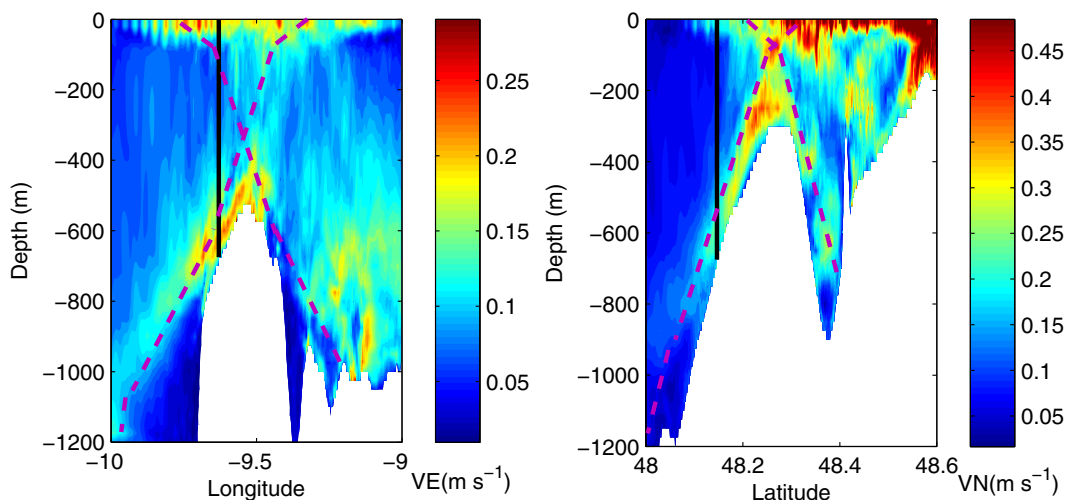
**Figure 13.** Model predicted amplitude of the (a) zonal and (b) meridional tidal velocities taken along the appropriate cross sections shown in Figure 7. The solid vertical line shows the position of the mooring St1. Characteristic lines are shown by magenta dashed curves.

the model output presented in Figure 13. The bottom intensification of the tidal currents at mooring St1 deployed in the place of the tidal beam origin (see Figure 4) was reproduced in the model time series (Figure 8).

## Appendix A: Internal Tides Over an Isolated Bank

MITgcm was applied to model an internal tide generated over a symmetric 30 km wide and 175 m high Gaussian bump situated in a basin of 250 m depth. The fluid stratification, tidal forcing, and all other model parameters were the same as in the main series of experiments. Figure A1 shows the plan view of generated internal waves in horizontal cross section at different stages of the tidal cycle. It is clear that the horizontal structure of the generated waves resembles a spiral-type wave that rotates clockwise. The wave is radiated from the seamount horizontally as described in the paper by *Baines* [2007]. Note that an analytical solution discussed in this paper is a linear one which does not allow any solitary waves. However, it is still good enough to capture the spiral character and evolution of the baroclinic tidal wave generation over a seamount.

In vertical directions, the internal waves generated over the Gaussian seamount resemble the property of the lowest baroclinic tidal mode with cophase displacement of isotherms, Figure A2. Two systems of nonlinear internal waves radiated from the seamount, i.e., the fragments A and B, are clearly seen in this figure on either side of the topography. In space, these waves are located in positions depicted in Figure A1 by similar letters. Looking at temperature cross sections (Figure A2), one assumes two independent wave systems radiating from the topography, however, the plan view in Figure A1 suggests that these wave fragments belong to the same spiral wave system.

## Appendix B: Internal Body Force

Corrugated bottom topography of the Celtic Sea shown in Figure 1 suggests generation of substantially three-dimensional internal wavefields. The simplest way to localize the potential sources of baroclinic tidal energy is to use a concept of the internal body force (IBF) introduced by *Baines* [1982].
Linear theory allows the problem of tidal energy conversion to be split into two governing systems of equations, barotropic and baroclinic [*Vlasenko et al.*, 2005]. The RHS of the baroclinic tidal wave system contains a term proportional to the vertical barotropic tidal velocity over an inclined bottom that drives
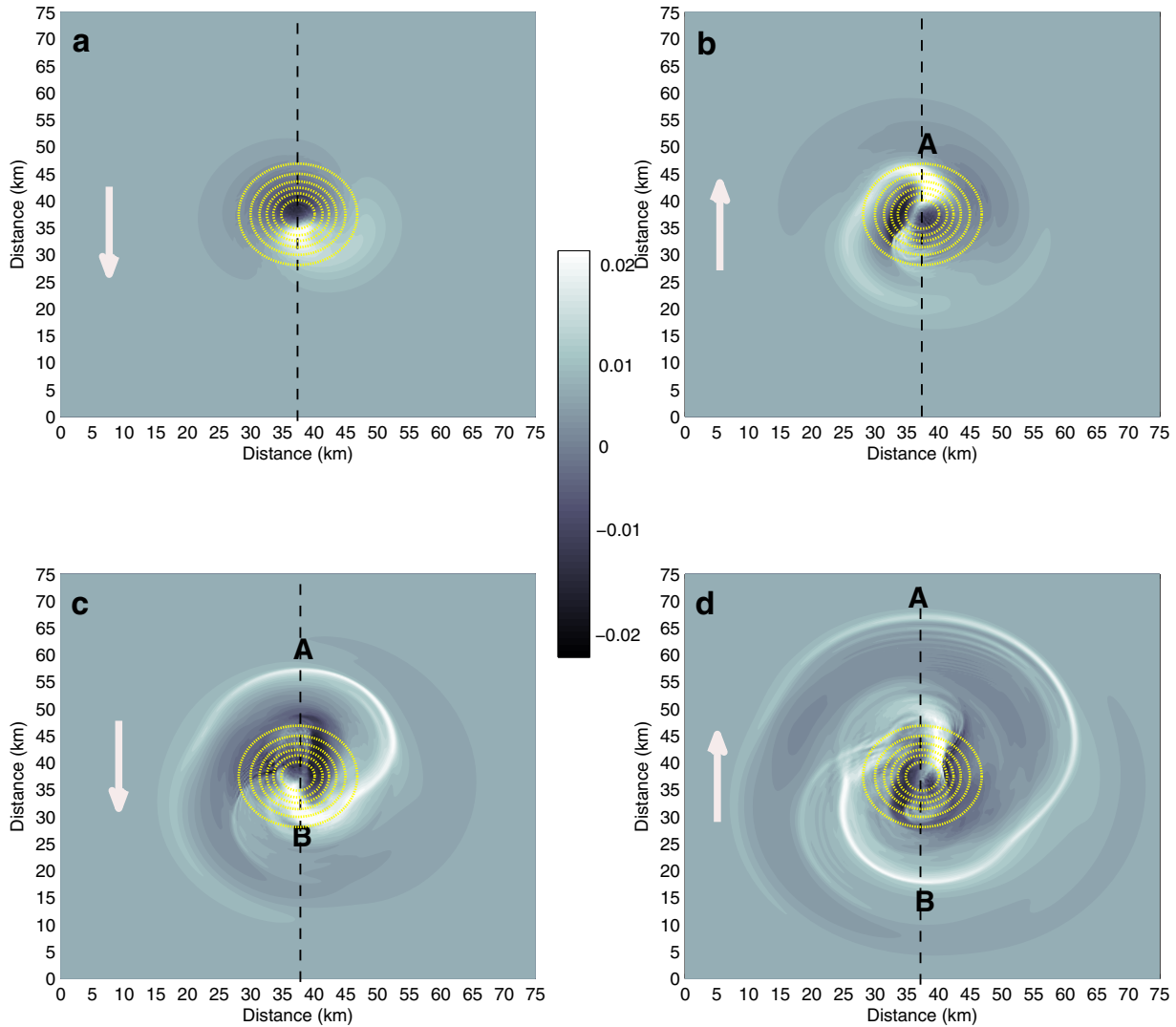
**Figure A1.** Plan view of a spiral-type internal wave system generated by semidiurnal tide over an isolated seamount. The sea-surface elevation displacement (in meters) produced by internal waves is presented in Figures A1a– A1d for 6, 12, 18, and 24 h, respectively. The white arrow shows the direction of the tidal flow. Yellow dotted lines show bottom topography.

the model and controls the location and intensity of the isopycnal displacements. In a two-dimensional ($x$, $z$) case, this term reads:

$$F = \rho_0 u_b H(x) z \frac{N^2(z)}{\sigma} \left( \frac{1}{H(x)} \right)_x.$$

Here $u_b$ is the amplitude of the barotropic tidal current; $H(x)$ is the bottom profile; $\sigma$ is the tidal frequency; $\rho_0$ is the reference density. Being integrated from the surface to the bottom, this formula gives an overall efficiency of the internal tide generation for the whole water column, $\Phi = \int_{-H}^{0} F dz$. In a three-dimensional case ($x$, $y$, $z$), the vertically integrated IBF in every point is calculated using the velocity $u_b$ and the derivative of the inverse depth in the direction perpendicular to the isobaths. The spatial distribution of the vertically integrated IBF $\Phi$ shown in Figure 12 was calculated for the stratification presented in Figure 2 and tidal forcing depicted in Figures 3 and 7.
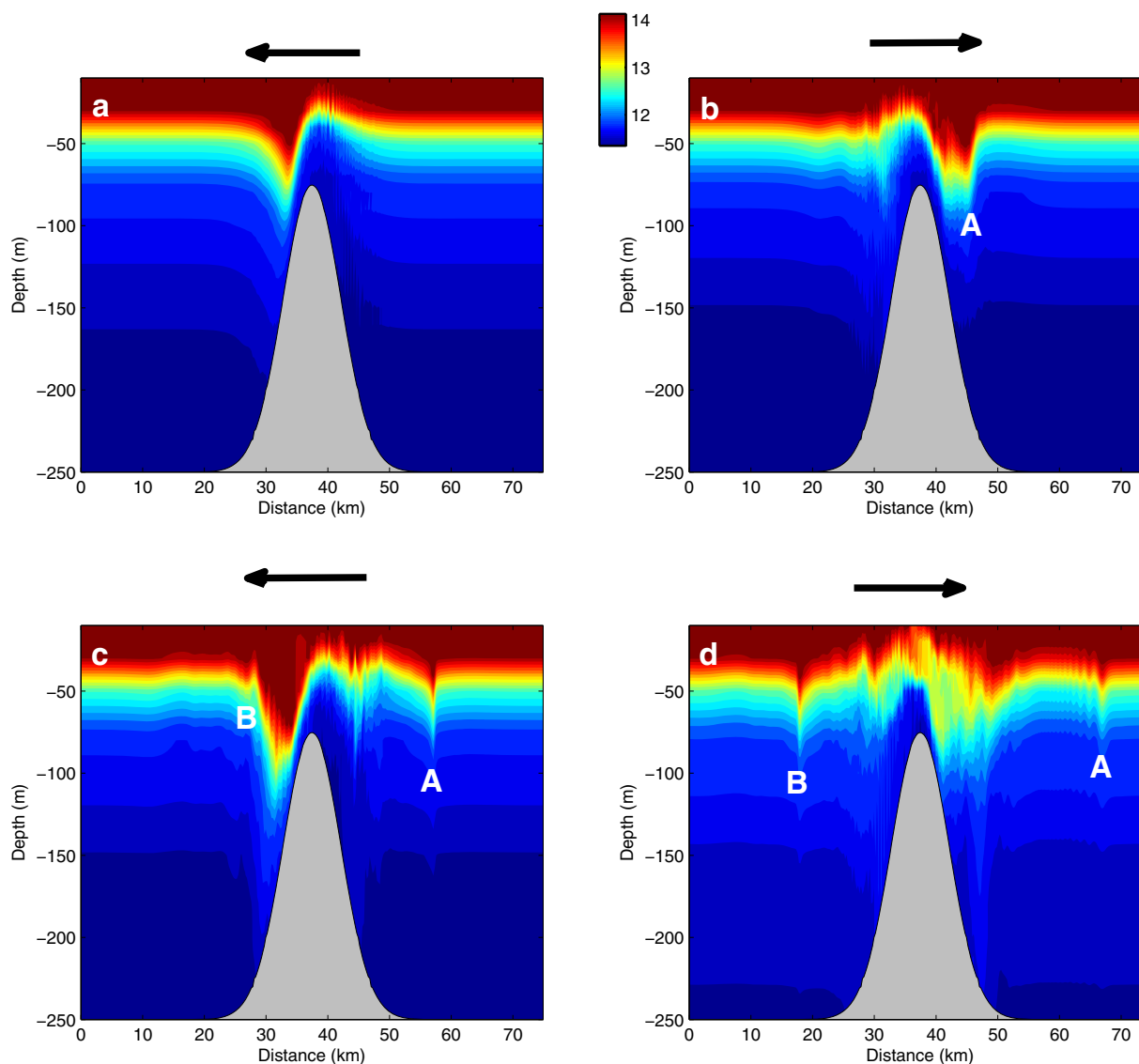
**Figure A2.** Vertical cross sections of temperature along the dashed lines shown in the appropriate plots of Figure A1. Positions of the strongest wavefronts are marked in both figures as A and B.

## References

Baines, P. G. (1982), On internal tide generation models, *Deep Sea Res., Part A*, *29*(3), 307–339.

Baines, P. G. (2007), Internal tide generation by seamounts, *Deep Sea Res., Part I*, *54*, 1486–1508.

Bruno, M., J. J. Alonso, A. Cózar, J. Vidal, A. Ruiz-Cañavate, F. Echevaria, and J. Ruiz (2002), The boiling-water phenomena at Camarinal Sill, the Strait of Gibraltar, *Deep Sea Res., Part II*, *49*, 4097–4113.

Farmer, D., Q. Li, and J.-H. Park (2009), Internal wave observations in the South China Sea: The role of rotation and non-linearity, *Atmos. Ocean*, *47*(4), 267–280.

Garrett, C., and E. Kunze (2007), Internal tide generation in the deep ocean, *Annu. Rev. Fluid Mech.*, *39*, 57–87.

Holt, J. T., and S. A. Thorpe (1997), The propagation of high frequency internal waves in the Celtic Sea, *Deep Sea Res., Part I*, *44*(12), 2087–2116.

Huthnance, J. M., H. Coelho, C. R. Griffiths, P. J. Knight, A. P. Rees, B. Sinha, A. Vangriesheim, M. White, and P. G. Chatwin (2001), Physical structures, advection and mixing in the region of Goban spur, *Deep Sea Res., Part II*, *48*(14–15), 2979–3021.

Egbert, G. D., and S. Y. Erofeeva (2002), Efficient inverse modeling of barotropic ocean tides, *J. Atmos. Oceanic Technol.*, *19*(2), 183–204.

Inall, M. E., D. Aleynik, T. Boyd, M. R. Palmer, and J. Sharples (2011), Internal tide coherence and decay over wide shelf sea, *Geophys. Res. Lett.*, *38*, L23607, doi:10.1029/2011GL049943.

Jackson, C. R., and J. R. Apel (2002), *An Atlas of Internal Solitary-Like Waves and Their Properties*, 229 pp., Off. of Nav. Res., Code 322PO, Alexandria, Va.

Marshall, J., A. Adcroft, C. Hill, L. Perelman, and C. Heisey (1997), A finite-volume, incompressible Navier-Stokes model for studies of the ocean on the parallel computers, *J. Geophys. Res.*, *102*, 5733–5752.

Osborne, A. R., and T. L. Burch (1980), Internal solitons in the Andaman sea, *Science*, *208*, 451–460.

Pacanowski, R. C., and S. G. H. Philander (1981), Parameterisation of vertical mixing in numerical models of Tropical Oceans, *J. Phys. Oceanogr.*, *11*, 1443–1451.

Pingree, R. D., and A. New (1995), Structure, seasonal development and sunglint spatial coherence of the internal tide on the Celtic and Armorican shelves and in the Bay of Biscay, *Deep Sea Res., Part I*, *42*, 245–284.

Pingree, R. D., and G. T. Mardell (1981), Slope turbulence, internal waves and phytoplankton growth at the Celtic Sea shelf-break, *Philos. Trans. R. Soc. London A*, *302*, 663–682.

Pingree, R. D., and G. T. Mardell (1985), Solitary internal waves in the Celtic Sea, *Prog. Oceanogr.*, *14*, 431–441.

Vlasenko, V., N. Stashchuk, and K. Hutter (2005), *Baroclinic Tides: Theoretical Modeling and Observational Evidence*, 351 pp., Cambridge Univ. Press, Cambridge.

Vlasenko, V., J. C. Sanchez Garrido, N. Stashchuk, J. G. Lafuente, and M. Losada (2009), Three-dimensional evolution of large-amplitude internal waves in the Strait of Gibraltar, *J. Phys. Oceanogr.*, *39*, 2230–2246.

Vlasenko, V., N. Stashchuk, M. Inall, and M. Palmer (2013), Generation of baroclinic tides over an isolated underwater bank, *J. Geophys. Res. Oceans*, *118*, 4395–4408, doi:10.1002/jgrc.20304.

Willmott, C. J. (1981), On the validation of models, *Phys. Geogr.*, *2*, 184–194.

Willmott, C. J. (1982), On the climatic optimization of the tilt and azimuth of flat-plane solar collectors, *Solar Energy*, *28*, 205–216.

Wesson, J. C., and M. C. Gregg (1994), Mixing at Camarinal Sill in the Strait of Gibraltar, *J. Geophys. Res.*, *99*, 9847–9878.